

# Time-Gated Polarization for Active Non-Line-Of-Sight Imaging

OSCAR PUEYO-CIUTAD, Universidad de Zaragoza, I3A, Spain

JULIO MARCO, Universidad de Zaragoza, I3A, Spain

STEPHANE SCHERTZER, French-German Research Institute of Saint-Louis, France

FRANK CHRISTNACHER, French-German Research Institute of Saint-Louis, France

MARTIN LAURENZIS, French-German Research Institute of Saint-Louis, France

DIEGO GUTIERREZ, Universidad de Zaragoza, I3A, Spain

ALBERT REDO-SANCHEZ, Universidad de Zaragoza, I3A, Spain

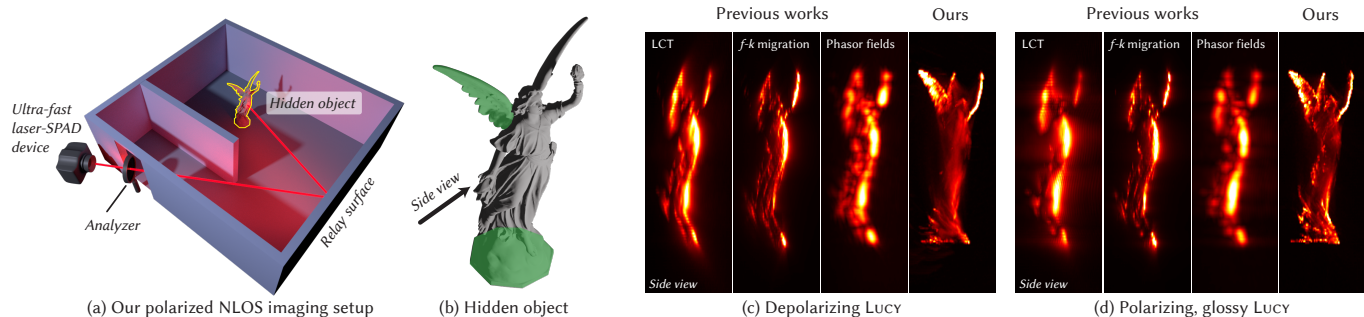


Fig. 1. (a) We propose a new technique for non-line-of-sight (NLOS) imaging that considers the polarization state of the captured light after the three bounce path of an unpolarized light pulse illuminating the relay surface. (b) Our method addresses a fundamental limitation of unpolarized NLOS methods, namely the *missing cone* problem: surfaces that are not placed in a specific position and orientation with respect to the relay surface cannot be imaged since they fall into the null-reconstruction space of the hidden object (highlighted in green). (c, d) Simulated reconstructions of Lucy with three unpolarized state-of-the-art NLOS methods (light-cone transform, f-k migration, and phasor fields) compared to the reconstruction of our method in which we can see features of target hidden object Lucy that could not be imaged previously, such as the base of the figure and the left wing. We leverage the directional information encoded in the polarization induced by the relay surface to reconstruct a Lucy made of a depolarizing material with diffuse reflectance (c), and a Lucy made of a polarizing material with higher glossiness (d). In both cases, our method provides highly detailed reconstructions, including features in the missing cone.

We propose a novel method to reconstruct non-line-of-sight (NLOS) scenes that combines polarization and time-of-flight light transport measurements. Unpolarized NLOS imaging methods reconstruct objects hidden around corners by inverting time-gated indirect light paths measured at a visible relay surface, but fail to reconstruct scene features depending on their position and orientation with respect to such surface. We address this limitation (known as the *missing cone* problem) by capturing the polarization state of light in time-gated imaging systems at picosecond time resolution, and introducing a novel inversion method that leverages directionality information of polarized measurements to reduce directional ambiguities in the reconstruction. Our method is capable of imaging features of hidden surfaces inside the missing cone space of state-of-the-art NLOS methods, yielding fine reconstruction details even when using a fraction of measured points on the relay surface. We demonstrate the benefits of our method in both simulated and experimental scenarios.

CCS Concepts: • **Computing methodologies** → **Computational photography**.

Additional Key Words and Phrases: non-line-of-sight imaging, time-of-flight imaging, polarimetric imaging, computational photography

## 1 INTRODUCTION

Time-gated non-line-of-sight (NLOS) imaging methods provide reconstructions of scenes hidden around corners by inverting the paths of light measured on a visible (relay) surface based on its time of flight [Buttafava et al. 2015; Lindell et al. 2019; Liu et al. 2019b;

O’Toole et al. 2018; Rapp et al. 2020; Velten et al. 2012; Xin et al. 2019]. While fundamental for many modern applications, solely relying on the time of flight of diffusely reflected light introduces ambiguities when estimating hidden surfaces due to the existence of multiple light paths with the same time of flight. Current approaches typically rely on filtering and feature extraction on either the input data or the output reconstruction to mitigate these ambiguities. However, they face a fundamental limitation: surfaces that do not retain a specific position and orientation with respect to the illuminated and captured points on the relay surface cannot be reconstructed (see Figure 1). This is known as the *missing cone problem* [Liu et al. 2019a], and such surfaces are said to be inside a *null-reconstruction space*.

In this work, we propose a novel NLOS imaging method that addresses the missing cone problem by leveraging *directional* information encoded in the polarization state of measured light. For this purpose, we formulate a new NLOS imaging model that considers polarization in the time-gated NLOS imaging capture process, and propose a novel inversion method that prunes the space of potential hidden points based on the directionality of polarization.

Our model considers a polarizing relay surface and its polarizing effect on the last bounce that directs the light to the detector. The polarization induced by the relay surface is due to the difference in the parallel and perpendicular components of the Fresnel reflection

coefficients with respect to the plane of incidence. The capture of the final polarization state allows us to reconstruct a depolarizing hidden object in confocal setups. For polarizing hidden objects, our model is capable of reconstructing them by leveraging the light path reversal properties of a confocal setup, even though these materials are commonly harder to image for conventional unpolarized methods. Notice that the only requirement for the capture configuration is that the detector must implement a polarization analyzer to measure the polarization state of the captured light.

In summary, our main contribution is the formulation of a polarimetric NLOS capture model and its inversion model, which allows us to reconstruct scene features inside the missing cone. As our results show (both simulated and experimental), our method recovers geometric features over the entire reconstruction space, including features that remained invisible to previous unpolarized NLOS imaging methods (see Figure 1), even with fewer sampling points on the relay surface than NLOS unpolarized methods. In particular, we show the extreme case of reconstructing a plane in the missing cone scanning only a single point on the relay surface, both in simulation and experimental captures.

## 2 RELATED WORK

NLOS imaging techniques are capable of extracting information of objects hidden around corners under a variety of operational and computational aspects [Faccio et al. 2020; Jarabo et al. 2017; Maeda et al. 2019]. While passive approaches typically rely on analyzing spatial gradients of indirect light measured with conventional cameras [Bouman et al. 2017; Klein et al. 2016; Saunders et al. 2019; Torralba and Freeman 2012], state-of-the-art results are governed by active methods based on ultra-fast time-gated illumination. At their core, these methods obtain 3D reconstructions of hidden objects by inverting the paths of indirect light measured at visible surfaces at picosecond temporal resolution [Arellano et al. 2017; Buttafava et al. 2015; Laurenzis and Velten 2014; Velten et al. 2012].

Time-gated NLOS imaging methods build upon this principle, increasing time efficiency by exploiting confocal capture setups [Lindell et al. 2019; O’Toole et al. 2018; Young et al. 2020], improving reconstruction quality through optimization and learning [Ahn et al. 2019; Choi et al. 2023; Iseringhausen and Hullin 2020; Mu et al. 2022; Plack et al. 2023; Shen et al. 2021; Tsai et al. 2017, 2019], using inexpensive sensors [Heide et al. 2013, 2014] or adding support for finer surfaces or non-diffuse reflectivity under more sophisticated capture systems [Xin et al. 2019]. Recent works unveiled analogies between time-gated NLOS imaging and wave-based image formation [Liu et al. 2020, 2019b], leading to a novel family of phasor-based methods operating in real-time [Guillén et al. 2020; Liao et al. 2021; Nam et al. 2021, 2020], and enabling new applications such as NLOS scene relighting [Marco et al. 2021] or imaging scenes around two corners [Royo et al. 2023].

However, despite the steady advances of time-gated methods in the last decade, their reliance on simplified light transport models leads to fundamental problems such as reconstruction ambiguities and limited surface visibility [Liu et al. 2019a]. This is known as the missing cone problem, one of the longstanding limitations of NLOS imaging techniques, which refers to the fact that certain scene

Table 1. Symbols used throughout this paper.

Symbol	Description
$l, d$	Laser and detector physical positions.
$x_l, x_d$	Laser and detector points on the relay surface.
$L, D$	Laser and detector scanned area on the relay surface.
$x_v$	Point in the hidden object $V$ .
$\tilde{x}$	Three-bounce path ( $l \rightarrow x_l \rightarrow x_v \rightarrow x_d \rightarrow d$ ).
$H(x_l, x_d, t)$	Unpolarized impulse response function from a laser point $x_l$ and capture point $x_d$ at time instant $t$ .
$S$	Stokes vector representing the polarization state.
$H_s(x_l, x_d, t, S)$	Stokes impulse response function.
$\xi, \psi$	Angle of linear polarization and degree of polarization.
$f(x_v)$	Albedo of $x_v$ .
$G(\tilde{x})$	Geometric attenuation of the path $\tilde{x}$ .
$\phi, \theta$	Azimuthal and incident angle.
$M(\tilde{x})$	Mueller matrix of a three-bounce-path $\tilde{x}$ .
$M(\theta^h)$	Reflection Mueller matrix in local plane of incidence with angle of incidence $\theta^h$ with respect to the microfacet normal $h$ .
$C_{h \leftarrow i}$	Rotation operation of polarization coordinate system in the Mueller-Stokes calculus. Rotates from the coordinate system $i$ to the coordinate system $h$ .
$R_{\perp}, R_{\parallel}$	Reflectance of the perpendicular and parallel components of the polarization with respect to the plane of incidence.

features cannot be accessed by NLOS measurements depending on their position and orientation with respect to the relay surface. Recent work by Royo et al. [2023] explored this issue by relying on fourth-bounce indirect photon paths, but requires particular combinations of secondary hidden planes to image surfaces invisible to third-bounce methods.

Recently, some works have incorporated polarization information, including passive NLOS imaging approaches [Liu et al. 2023; Tanaka et al. 2020]. Polarization and time-gated detectors have been combined to recover the full spatio-temporal polarimetric response of a scene [Baek and Heide 2021], infer geometric and material properties based on the temporal evolution of polarimetric reflected light [Baek and Heide 2022], estimate depth through scattering media [Jeon et al. 2023; Wu et al. 2018], or to identify light coming from a secondary relay surface for multi-view reconstructions [Wang et al. 2024]. In contrast, we incorporate polarization into time-gated active NLOS imaging to recover directionality information of light reaching the detector. This allows us to address the missing cone problem and reconstruct surfaces in the null-reconstruction space of previous methods.

## 3 BACKGROUND

### 3.1 Non-line-of-sight imaging

Typical time-resolved NLOS imaging setups implement active capture systems composed of a laser at a position  $l$  and a detector at a position  $d$ , both facing a visible relay surface and lacking direct line of sight to the hidden object to be reconstructed (see Figure 2a, left, for a confocal example where  $l \equiv d$ ). During the capture process,

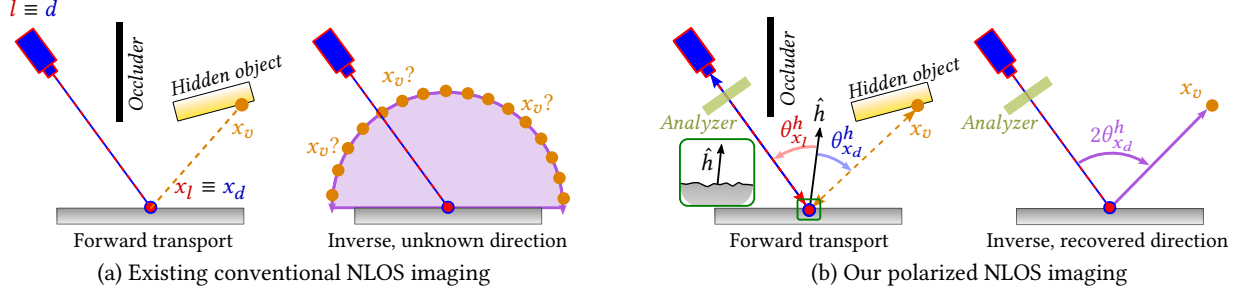


Fig. 2. Schematic comparing an unpolarized NLOS method and our method leveraging directional information encoded in the polarization. (a) Unpolarized NLOS light transport model depicted as a confocal setup for simplicity. (a, left) The light emitted by laser  $l$  travels along path  $\langle l \rightarrow x_l \rightarrow x_v \rightarrow x_d \rightarrow d \rangle$  before reaching detector  $d$ . Both laser  $l$  and detector  $d$  are coaxial and aim at the same point of the relay surface. (a, right) When inverting a model in unpolarized methods, the only information of the measured light is its time of flight and, hence, all the possible candidates  $x_v$  lie on a hemisphere with radius  $c\Delta t_v/2$ . As a result, there is no definite recoverable direction. (b) Our polarized NLOS transport model, also depicted as a confocal setup for simplicity. (b, left) We analyze the polarizing effects of a conductive, micro-faceted relay wall to retrieve directional information. (b, right) If the hidden object is depolarizing, we invert the polarizing effect of the last bounce to determine the direction of the ray and, hence, recover the direction to  $x_v$ . Note that the analyzer is only placed in front of the detector.

ultra-fast laser light pulses illuminate a set of points  $x_l$  on the visible relay surface. For every illuminated point  $x_l$ , the detector measures the time-resolved indirect light produced by the hidden object at a set of points  $x_d$  on that same relay surface.

The result of this process is a discretized time-resolved signal that approximates the impulse response function  $H(x_l, x_d, t)$  of the hidden object to a delta illumination pulse  $\delta(x_l, t)$ . NLOS imaging methods assume that the impulse response function only includes three-bounce illumination under diffuse surface reflectance and no occlusions, for which the impulse response function is defined as:

$$H(x_l, x_d, t) = \int_V f(x_v)G(\tilde{x})\delta(t - \Delta t_v)dx_v \quad (1)$$

where  $x_v \in V$  are surface points of the hidden object  $V$ ;  $f(x_v)$  models the albedo of such points;  $G(\tilde{x})$  represents the geometric attenuation of the three-bounce path  $\tilde{x} = \langle l \rightarrow x_l \rightarrow x_v \rightarrow x_d \rightarrow d \rangle$ ; and  $\Delta t_v = \frac{\|x_v - x_l\| + \|x_d - x_v\|}{c}$  is the time of flight of such paths at the speed of light  $c$ , as  $H$  is typically time-normalized at the relay surface, i.e., the time of flight of  $l \rightarrow x_l$  and  $x_d \rightarrow d$  sub-paths is subtracted from the time of flight  $t$  of captured photons during calibration.

After capturing the impulse response function  $H$ , NLOS imaging methods typically reconstruct the hidden object by estimating the albedo  $f$  of point  $x_v$  as:

$$f(x_v) \approx K(x_v) * \int_D \int_L H(x_l, x_d, \Delta t_v)dx_l dx_d \quad (2)$$

which approximates an inverse of three-bounce paths with time of flight  $\Delta t_v$  back to hidden object locations  $x_v$  (see Figure 2a, right),  $K(x_v)$  represents a spatial filter over the result of the integral in Equation (2), and  $\int_D dx_d$  and  $\int_L dx_l$  integrate over all the illuminated and measured points. Alternatively, a temporal filter  $K(t)$  may be used over the temporal domain of  $H$ , so the integrand becomes  $H'(x_l, x_d, t) = K(t) * H(x_l, x_d, t)$  [Liu et al. 2019b]. Existing NLOS imaging works provide efficient solvers, alternative formulations, and filtering strategies for this inversion process [Ahn et al. 2019; Buttafava et al. 2015; Lindell et al. 2019; Liu et al. 2019b; O'Toole et al. 2018; Velten et al. 2012].

### 3.2 Polarization

Our work exploits additional information contained in the polarization of light to improve the reconstruction of hidden objects. The Stokes vector  $\mathbf{S} = (S_0, S_1, S_2, S_3)^T$  describes such polarization, where  $S_0$  represents the total intensity of light, and  $S_1, S_2$ , and  $S_3$  are the polarized components defined by the degree of polarization  $\psi$ , angle of linear polarization  $\xi$ , and ellipticity angle  $\zeta$ :

$$\mathbf{S} = S_0 \begin{pmatrix} 1 & \psi \cos 2\zeta \cos 2\xi & \psi \cos 2\zeta \sin 2\xi & \psi \sin 2\zeta \end{pmatrix}^T \quad (3)$$

$S_1, S_2$ , and  $S_3$  describe horizontal, linearly diagonal, and circular polarization, respectively. The linear components of the Stokes vector can be obtained from measurements as:

$$\mathbf{S} = (I_0 + I_{90} \quad I_0 - I_{90} \quad I_{45} - I_{135} \quad 0)^T \quad (4)$$

where each  $I_\alpha$  represents the intensity of the light beam transmitted through a linear polarizer oriented at an angle  $\alpha$ . In our work, we do not capture circular polarization and, hence,  $S_3 = 0$ .

The polarization state of light is transformed by polarization transformation events as  $\mathbf{S}_a = M\mathbf{S}_b$ , where  $M$  is a Mueller matrix, and  $\mathbf{S}_a, \mathbf{S}_b$  are the Stokes vectors after and before the transformation event defined by  $M$ . Before an interaction, the axes must be aligned to the plane of incidence, which requires a rotation of the local coordinate system. A counterclockwise rotation of the axis by an angle  $\phi$  is represented by the following matrix:

$$C(\phi) = \begin{pmatrix} 1 & 0 & 0 & 0 \\ 0 & \cos 2\phi & \sin 2\phi & 0 \\ 0 & -\sin 2\phi & \cos 2\phi & 0 \\ 0 & 0 & 0 & 1 \end{pmatrix} \quad (5)$$

For a more in-depth description of polarized light, we refer the reader to the work by Wilkie and Weidlich [2012].

### 3.3 The missing cone problem

In time-gated NLOS imaging, the missing cone problem refers to the decrease of performance when reconstructing surfaces at specific positions and orientations with respect to the capture baseline—i.e., laser and detector targets on the relay surface—even though

such surfaces scatter light from laser targets to sensing targets on the relay surface Liu et al. [2019a]. This problem has been studied in different imaging fields, such as computed tomography [Benning et al. 2015; Delaney and Bresler 1998], 3D microscopy [Mertz 2019], and optical diffraction tomography [Lim et al. 2015], under a frequency-domain perspective.

In an NLOS imaging system, the impulse response function  $H$  measures a spatio-temporal projection of light reflected by the hidden objects over the relay surface. For an NLOS imaging system to be able to reconstruct a surface with sufficient resolution, the Fourier transform of the captured data  $H$  should exhibit a strong signal at frequencies proportional to such resolution. For surfaces at specific orientations with respect to the capture baseline, the signal intensity of high spatio-temporal frequencies tends to decrease to zero, with lower frequencies dominating the spectrum of  $H$ . This phenomenon is demonstrated by the Fourier slice theorem. While reconstructing such planes under dominating lower imaging frequencies—those with a higher signal in the Fourier transform of  $H$ —is in principle possible, the reconstruction resolution becomes too coarse.

## 4 METHOD

In conventional unpolarized NLOS methods, impulse response functions encode only the optical distance traveled by captured photons (see Figure 2a, left). As a result, existing inverse models suffer from directional ambiguities since all the possible candidate points that could have reflected such photons lie on an ellipsoidal manifold (spherical if the capture setup is confocal, see Figure 2a, right). To address this issue, we make the observation that polarization encodes light directionality. We thus extend the impulse response function to capture the polarization state of light, and propose a novel method that leverages polarized impulse response functions to mitigate directional ambiguities.

We first reformulate the classic NLOS transport model expressed by Equation (1) to include polarization effects, resulting in our *polarized NLOS forward model* in Section 4.1. We then show how the directionality of light reflected from the depolarizing hidden object can be recovered from the polarizing effects introduced by the relay surface (Figure 2b, left), and derive our closed-form inversion model in Section 4.2 (Figure 2b, right). Last, in Section 4.3 we adapt our model to handle polarizing hidden objects, such as metallic surfaces, which are hard to image using conventional methods due to their increased specular reflectance.

### 4.1 Polarized NLOS forward model

Conventional impulse response functions  $H(x_l, x_d, t)$  capture only the intensity of light, ignoring its polarization state. We first aim to extend  $H$  to include polarization, which will allow us to constrain the set of points in the scene that reflected light with a specific time of flight based on its polarization state. We reformulate the forward transport model expressed by Equation (1) as:

$$H_s(x_l, x_d, t, \mathbf{S}) = \int_V G(\tilde{x}) f(x_v) M(\tilde{x}) \mathbf{S}_l \delta(t - \Delta t_v) dx_v \quad (6)$$

where  $\mathbf{S}$  represents the Stokes vector of the polarization state of the light reaching the detector,  $M(\tilde{x})$  is the Mueller matrix encoding the

polarization events through the three-bounce path  $\tilde{x}$ , and  $\mathbf{S}_l$  is the Stokes vector representing the polarization state of the laser source. We name  $H_s$  the *Stokes impulse response function*.

The Mueller matrix  $M(\tilde{x})$  is composed by the Mueller matrices associated to each bounce in  $\tilde{x}$  and the change in the coordinate system  $C$  to align the plane of incidence at each bounce (see Section 3.2):

$$M(\tilde{x}) = C_{d \leftarrow x_d} M_{x_d} C_{x_d \leftarrow x_v} M_{x_v} C_{x_v \leftarrow x_l} M_{x_l} C_{x_l \leftarrow l} \quad (7)$$

where  $M_{x_i}$  is the Mueller matrix at the reflection point  $x_i$  ( $i \in \{l, v, d\}$ ), and  $C_{x_2 \leftarrow x_1}$  rotate the polarization coordinate system from the initial coordinate system of  $x_1$  to the final coordinate system of  $x_2$ . Mueller matrices  $M$  and rotation matrices  $C_{x_2 \leftarrow x_1}$  modify the polarization of light, independent of its intensity. The polarization state depends on three factors: i) the polarimetric properties of materials, ii) the incoming and outgoing directions of light reaching the surface, and iii) the plane of incidence.

Our final goal is to provide an inverse of Equation (6), to be able to reconstruct the hidden object. We incorporate angular discrimination as:

$$f(x_v) \approx \int_D \int_L H_s(x_l, x_d, \Delta t_v, \mathbf{S}_0) \delta(H_s(x_l, x_d, \Delta t_v, \mathbf{S}) - M(\tilde{x}) \mathbf{S}_l) dx_l dx_d \quad (8)$$

where  $H_s(x_l, x_d, \Delta t_v, \mathbf{S}_0)$  represents intensity, and  $\delta(\cdot)$  incorporates such angular discrimination by constraining the integrated value at  $x_v$  to a three-bounce path  $\tilde{x}$ , whose expected polarization state matches the state captured by  $H_s$ .

Solving Equation (8) is ill-posed since it involves three independent polarizing events (i.e., bounces at  $x_l$ ,  $x_v$  and  $x_d$ ) including unknown polarimetric properties and geometry of the hidden object, as well as a rotation of the polarization coordinate system to align polarization components to the plane of incidence. The combination of the three Mueller matrices with said unknowns leads to different possible solutions for every scanned point  $x_d$  on the relay surface.

However, for a point  $x_v$  in a general depolarizing hidden object, the Mueller matrix is:

$$M_{x_v} = \begin{pmatrix} 1 & 0 & 0 & 0 \\ 0 & 0 & 0 & 0 \\ 0 & 0 & 0 & 0 \\ 0 & 0 & 0 & 0 \end{pmatrix} \quad (9)$$

which allows us to simplify Equation (7) into:

$$M(\tilde{x}) = C_{d \leftarrow x_d} M_{x_d} M_{x_v} \quad (10)$$

Since the hidden geometry depolarizes light ( $M_{x_v}$ ), all the previous polarization terms  $C_{x_v \leftarrow x_l} M_{x_l} C_{x_l \leftarrow l}$  and the rotation of the linear component  $C_{x_d \leftarrow x_v}$  can be ignored. Equation (10) allows us to define a simpler Stokes impulse response function  $H_s$  as:

$$H_s(x_l, x_d, t, \mathbf{S}) = \int_V G(\tilde{x}) f(x_v) C(-\phi) M_{x_d} \mathbf{S}_u \delta(t - \Delta t_v) dx_v \quad (11)$$

where the unpolarized scattered light from the hidden object  $\mathbf{S}_u$  is only transformed by the Mueller matrix  $M_{x_d}$  of the last bounce, followed by a change in the polarization coordinate system  $C_{d \leftarrow x_d} \equiv C(-\phi)$  to align the plane of incidence to the detector reference system.

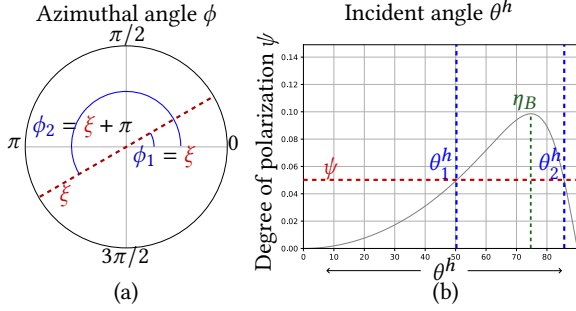


Fig. 3. (a) Two possible solutions for the azimuth  $\phi = \{\xi, \xi + \pi\}$ , and (b) two possible solutions for the incident angle  $\theta^h$  around the pseudo-Brewster angle  $\eta_B$ ; calculated from the angle of linear polarization  $\xi$  and the degree of polarization  $\psi$  respectively. The combination of  $(\phi_1, \phi_2) \times (\theta_1^h, \theta_2^h)$  yields four possible solutions, but we discard the solutions including  $\theta_2^h$  because the angles fall behind the relay surface.

#### 4.2 Inverting our model

Based on our forward model in Equation (11), we now aim to build an inverse model to exploit the directionality of light scattered by a polarizing relay surface (see Figure 2b, left) and reduce the candidate directions of inverted paths (see Figure 2b, right). For convenience, we describe the polarizing effects of the relay surface with a microfacet model [Beckmann and Spizzichino 1963].

Polarization effects in a microfacet model occur in the plane of incidence of the reflection. They are described by the Fresnel equations, which indicate that light polarized in the axis parallel to the plane of incidence is affected differently than light polarized perpendicularly to such plane. The reflection Mueller matrix is given by:

$$M(\theta^h) = \frac{1}{2} \begin{pmatrix} R_{\perp} + R_{\parallel} & R_{\perp} - R_{\parallel} & 0 & 0 \\ R_{\perp} - R_{\parallel} & R_{\perp} + R_{\parallel} & 0 & 0 \\ 0 & 0 & 2\sqrt{R_{\perp}R_{\parallel}} \cos \Delta_p & -2\sqrt{R_{\perp}R_{\parallel}} \sin \Delta_p \\ 0 & 0 & 2\sqrt{R_{\perp}R_{\parallel}} \sin \Delta_p & 2\sqrt{R_{\perp}R_{\parallel}} \cos \Delta_p \end{pmatrix} \quad (12)$$

where  $R_{\perp}$  and  $R_{\parallel}$  are the reflection coefficients for the perpendicular and parallel components of the polarization with respect to the incident plane, and  $\Delta_p$  is the delay on phase shift, which depends on the complex refractive index and angle of incidence  $\theta^h$  with respect to the microfacet normal  $h$ .

Assuming that light with time of flight  $t$  captured in  $H_s(x_l, x_d, t, S)$  was reflected by a single point  $x_v$  in the hidden object<sup>1</sup>, we obtain the direction from  $x_d$  in the relay surface to  $x_v$  through the estimation of the microfacet normal  $\hat{h}$  for each transient bin. Note that the relay surface scatters light towards all directions, but the polarization state of reflected light from points  $x_v$  at different distances from  $x_d$  is captured with different times of flight.

Under this assumption, we can replace the integrand over the volume  $V$  in Equation (11) with the contribution of a single-point,

<sup>1</sup>Note that we refer to light reflected by a finite surface area centered at  $x_v$ , not by an infinitesimal mathematical point. Such area can be safely considered sufficiently small compared to the scene size.

and  $M_{x_d} = M(\theta_{x_d}^h)$  (see Figure 2b, left) under the microfacet model:

$$H_s(x_l, x_d, t, S) = \frac{G(\tilde{x})f(x_v)}{2} \begin{pmatrix} R_{\parallel} + R_{\perp} \\ (R_{\perp} - R_{\parallel}) \cos(2\phi) \\ (R_{\perp} - R_{\parallel}) \sin(2\phi) \\ 0 \end{pmatrix} \quad (13)$$

We provide a step-by-step derivation in the supplemental document.

The captured Stokes vector (in brackets) shows that the angle of linear polarization  $\xi = \frac{1}{2} \tan^{-1}(S_2, S_1)$  depends on the azimuthal angle  $\phi$  through the rotation  $C(-\phi)$  (terms  $\cos(2\phi)$  and  $\sin(2\phi)$ ). The degree of polarization  $\psi = \sqrt{S_1^2 + S_2^2}/S_0$  depends on the angle of incidence  $\theta^h$  of the bounce in the relay through the Mueller matrix  $M(\theta_{x_d}^h)$  (terms  $R_{\perp}$  and  $R_{\parallel}$ ).

We invert Equation (13) constraining backprojection by leveraging the polarization state of the captured light. The angle of linear polarization  $\xi$  constrains the azimuthal angle  $\phi$ , whereas the degree of polarization  $\psi$  constrains the incidence angle  $\theta^h$ :

$$f(x_v) \approx \int_D \int_L H(x_l, x_d, \Delta t_v, S_0) \delta(\xi(H_s(x_l, x_d, \Delta t_v, S)) - \xi(S_d)) \delta(\psi(H_s(x_l, x_d, \Delta t_v, S)) - \psi(S_d)) dx_l dx_d \quad (14)$$

where  $\int_D \int_L dx_l dx_d$  integrates over the polarization state of all  $x_l$  and  $x_d$  points, and  $S_d = M(\tilde{x})S_l$ . Due to the simplified model from Equation (10), we can compute the expected polarization state  $S_d$ . Note that this inversion does not require prior knowledge of the normals in the hidden geometry, nor attempts to estimate them, since we only exploit the polarization state of reflected light.

Given the above, we next show how this formulation allows us to reduce the candidate directions (see Figure 2b, right), and how these can be computed directly based on the polarization state. This eliminates the need of having to reconstruct a certain volume and then check which parts of the signal match the expected angle of linear polarization  $\xi$  and degree of polarization  $\psi$ . Our method recovers the candidate microfacet normal  $\hat{h}$  that caused the reflection. In particular, we map the polarization state to spherical coordinates  $(\phi, \theta)$  and recover  $\hat{h} = (\sin \theta^h \cos \phi, \sin \theta^h \sin \phi, \cos \theta^h)$  by computing the azimuth angle  $\phi$  from the angle of linear polarization  $\xi$ , and the angle of incidence  $\theta^h$  from the degree of polarization  $\psi$ .

We recover a total of four candidate solutions (depicted in Figure 3) as possible directions that lead to the captured polarization state. The azimuthal angle  $\phi$  has two possible solutions from the angle of linear polarization (Figure 3a):  $\phi \in \{\xi, \xi + \pi\}$ . The angle of incidence  $\theta^h$  also has two possible solutions from the degree of polarization  $\psi$  around the pseudo-Brewster's angle (Figure 3b), which we obtain by building a look-up table mapping  $\psi \rightarrow \{\theta_1^h, \theta_2^h\}$ . The set of four possible solutions from the polarization state corresponds to the possible directions (combinations of  $\{\phi_1, \phi_2\}$  and  $\{\theta_1^h, \theta_2^h\}$ ) that light could have followed. However, the two solutions corresponding to  $\theta_2^h$  are not considered, since the candidate directions fall behind the relay (see Figure 3b).

Then, we obtain the outgoing direction  $x_d \rightarrow x_v$  by tracing the specular reflection of the incident vector  $d \rightarrow x_d$  with respect to

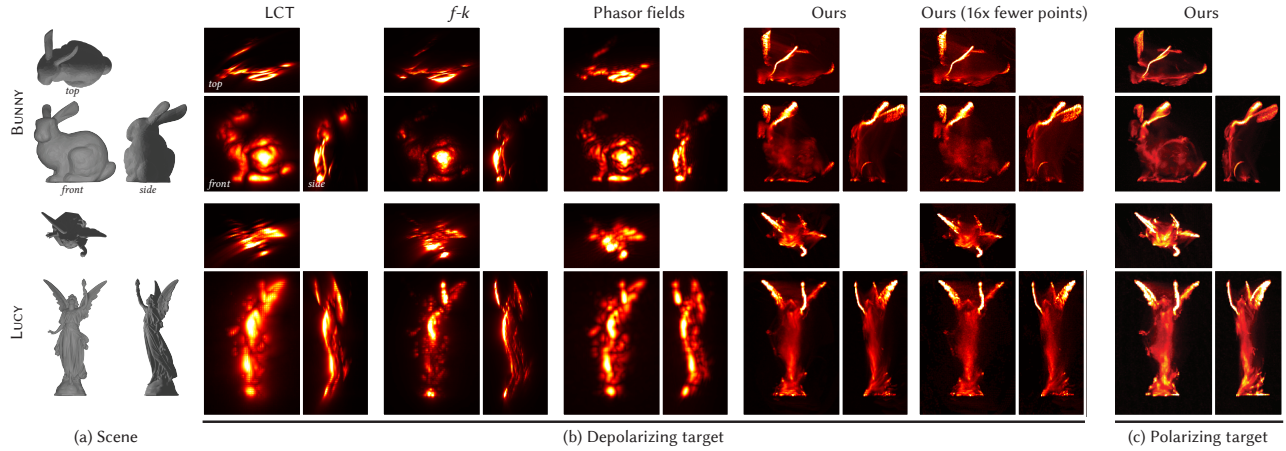


Fig. 4. Simulated results comparing reconstructions of BUNNY and LUCY. Previous works (LCT [O’Toole et al. 2018],  $f$ - $k$  migration [Lindell et al. 2019], phasor fields [Liu et al. 2019b]) fail to reconstruct certain features when they fall into the missing cone (e.g., BUNNY’s ears, LUCY’s wings and base). By leveraging polarization, our method yields full reconstructions even when using 16 times less scanned points (without decrease in quality, but reducing reconstruction time). As shown in (c), our method also produces high-quality reconstructions in the presence of polarizing rough conductors materials for the hidden object.

the recovered microfacet normal  $\hat{h}$ . We achieve this with the spherical coordinates of  $\overline{x_d x_v} = (\sin 2\theta^h \cos \phi, \sin 2\theta^h \sin \phi, \cos 2\theta^h)$ . We recover the point  $x_v$  in the hidden object that reflected the light to the relay surface as  $x_v = x_d + \overline{x_d x_v} \frac{c\Delta t_v}{2}$  combined with the time of flight  $\Delta t_v$  (in a confocal setup). Although the reconstructed point cloud can be visualized directly, we voxelize the hidden object and compute every voxel value as the sum of all reconstructed points contained within such voxel for comparison purposes.

### 4.3 Polarized NLOS on polarizing hidden object

In the previous section we explained how we can extract directionality in the general case when the hidden geometry depolarizes light. However, we can also adapt our formulation for cases where such hidden geometry is made of a polarizing material, which is hard to image with existing techniques.

*Forward model.* We rely on a confocal setup, where  $x_l \equiv x_d$ ,  $l \equiv d$ , the path from  $l$  to  $x_l$  is co-axial to the path from  $d$  to  $x_d$ , and the path from  $x_l$  to  $x_v$  is co-axial to the path from  $x_d$  to  $x_v$  (see Figure 2a). This yields three important observations (see Figure 2b, left):

- (1) Light is only polarized linearly, since all the light bounces lie on the same plane of incidence and we initially illuminate the relay surface with unpolarized light.
- (2) The first and the third bounce on the relay surface at  $x_l$  and  $x_d$  produce the same polarizing effect, since they have the same angle of incidence. This implies that  $\theta_{x_l}^h = \theta_{x_d}^h$  and therefore,  $R_{\perp}^{x_l} = R_{\perp}^{x_d}$  and  $R_{\parallel}^{x_l} = R_{\parallel}^{x_d}$ .
- (3) The hidden object does not modify polarization, since in a confocal path the reflected angle  $\theta_{x_v}^h$  with respect to the average angle of the microfacet distribution is zero. This implies that  $R_{\perp}^{x_v} = R_{\parallel}^{x_v}$ . Since light is only polarized linearly, phase shifts can be ignored.

These observations imply that  $M(\theta_{x_d}^h) = M(\theta_{x_l}^h)$ , since  $x_l \equiv x_d$  share the same angle of incidence;  $C_{x_v \leftarrow x_l} = C_{x_d \leftarrow x_v} = \mathbf{I}$  (identity

matrix), since the bounces in the relay surface and the hidden object share the plane of incidence; and  $M(\theta_{x_v}^h = 0) = \mathbf{I}$ , since the phase shift does not affect linear polarization within the plane of incidence. Moreover, the  $C_{x_l \leftarrow l}$  term is unnecessary since the emitted light is unpolarized, so only the third bounce introduces a rotational change in the coordinate system  $C_{d \leftarrow x_d}$ . As a result, the Mueller matrix (Equation (7)) becomes:

$$M(\tilde{x}) = C_{d \leftarrow x_d} M(\theta_{x_d}^h) M(\theta_{x_l}^h) = C(-\phi) M(\theta_{x_d}^h)^2 \quad (15)$$

where  $C(-\phi)$  is the rotation needed to align to the detector’s coordinate system. The Mueller matrix of the three-bounce path with polarizing geometry is similar to the Mueller matrix with depolarizing geometry from Equation (10), but replacing the depolarizing matrix by  $M(\theta_{x_l}^h)$ , leading to the squared term  $M(\theta_{x_d}^h)^2$ .

*Inverse model.* Following a similar derivation as in the case of depolarizing hidden geometry, and assuming again that light is only reflected from one point of the hidden object, the captured polarization state corresponds to (see Supplementary for details):

$$H_s(x_d, t, \mathbf{S}) = \frac{G(\tilde{x})f(x_v)}{2} \begin{pmatrix} R_{\parallel}^2 + R_{\perp}^2 \\ (R_{\perp}^2 - R_{\parallel}^2) \cos(2\phi) \\ (R_{\perp}^2 - R_{\parallel}^2) \sin(2\phi) \\ 0 \end{pmatrix} \quad (16)$$

where  $H_s$  is now a three-parameter function since  $x_l \equiv x_d$ . This formulation can be inverted as described in Section 4.2, with the only difference that the mapping  $\psi \rightarrow \{\theta_1^h, \theta_2^h\}$  is built from the degree of polarization of  $M(\theta_{x_d}^h)^2$  instead of  $M(\theta_{x_d}^h)$ .

## 5 EXPERIMENTAL VALIDATION

### 5.1 Simulation results

We first evaluate our method in synthetic NLOS scenarios using transient path tracing techniques optimized for NLOS imaging [Jarabo et al. 2014; Royo et al. 2022] built over MITSUBA 3 [Jakob et al. 2022]

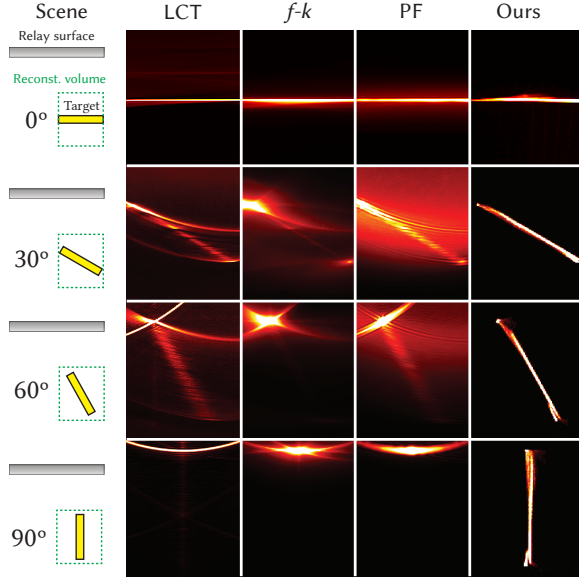


Fig. 5. Top views of the simulated reconstruction of a single, isolated plane at different orientations with respect to the relay surface, comparing previous works and our method in simulation. For previous methods (LCT,  $f$ - $k$ , and phasor fields) we scan  $128 \times 128$  points of the relay surface, and only  $32 \times 32$  for ours. At  $0^\circ$ , previous methods reconstruct correctly the plane. However, as the plane rotates and enters in the null-reconstruction space, previous methods progressively fail to reconstruct the plane, while we consistently yield good results. At  $90^\circ$  (completely in the missing cone), our method is the only one capable of reconstructing the plane correctly. Note that the work from Royo et al. [2023] relies on fourth-bounce illumination, which is not present in this scene, and thus it can not be applied.

with polarization. We test our method for both depolarizing and polarizing hidden objects. We model the polarizing relay surface with a Beckmann microfacet distribution with a roughness of  $\alpha = 0.9$ , resembling our experimental aluminum relay surface (Section 5.2); the high value of the roughness coefficient ensures a close-to-diffuse reflectance. We scan a region on the relay surface of  $1 \text{ m} \times 1 \text{ m}$ . The detector has a temporal resolution of 10 ps. We binarize the impulse response function to weigh equally light from low-contribution parts of the hidden object. We simulate all the scenarios in a confocal setup, but our method is not constrained to this particular configuration.

*Stokes impulse response function.* We evaluate and compare the results of our method against three state-of-the-art methods: LCT [O’Toole et al. 2018],  $f$ - $k$  migration [Lindell et al. 2019], and phasor fields [Liu et al. 2019b]. For a fair comparison we scan a square grid of  $128 \times 128$  confocal points on the relay surface for all methods. We also test our method with  $32 \times 32$  confocal points and the four captures required to recover the polarization state of the light for each confocal point. The reconstructions in Figure 4 show how previous methods fail when reconstructing certain parts of the hidden objects that fall within the missing cone, such as the ears and silhouette of BUNNY, or the left wing and base of LUCY. In

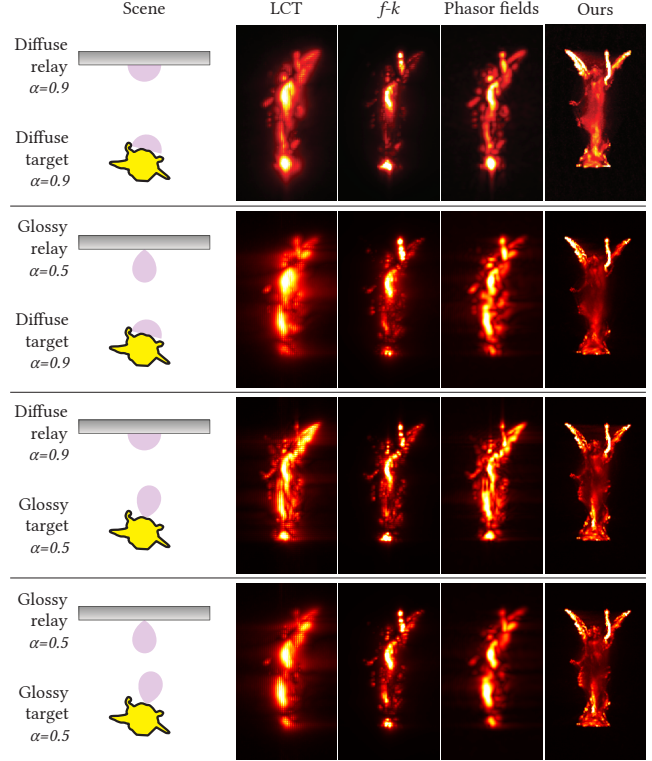


Fig. 6. Comparison of our method with previous works under different glossiness levels of the relay surface and target Lucy (hidden object), using polarizing rough conductors with  $\alpha = 0.9$  (diffuse reflectance) and  $\alpha = 0.5$  (glossy reflectance). Our method yields consistent quality regardless of the surface reflectance, while previous works noticeably degrade when surfaces are not diffuse, specially when increasing glossiness of the relay surfaces (second and fourth rows).

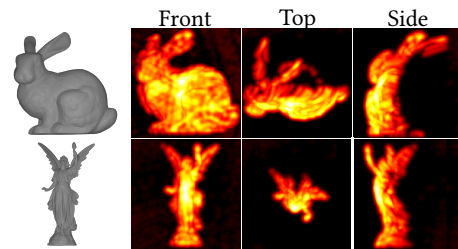


Fig. 7. Reconstruction of BUNNY and LUCY simulating non-colliding polarization states by exhaustively discretizing the polarization dimensions into 314 angles of linear polarization  $\xi$  and 500 degrees of polarization  $\psi \in [0, 0.075]$  bins for each point, scanning only four confocal points on the relay surface. Under this simulation, all scene features are clearly visible in the reconstructions, including those in the missing cone (BUNNY’s ear, or LUCY’s wing). The separation of light paths by their polarization state effectively adds an angular dimension to the reconstructions. See the Supplementary for a detailed description of this formulation.

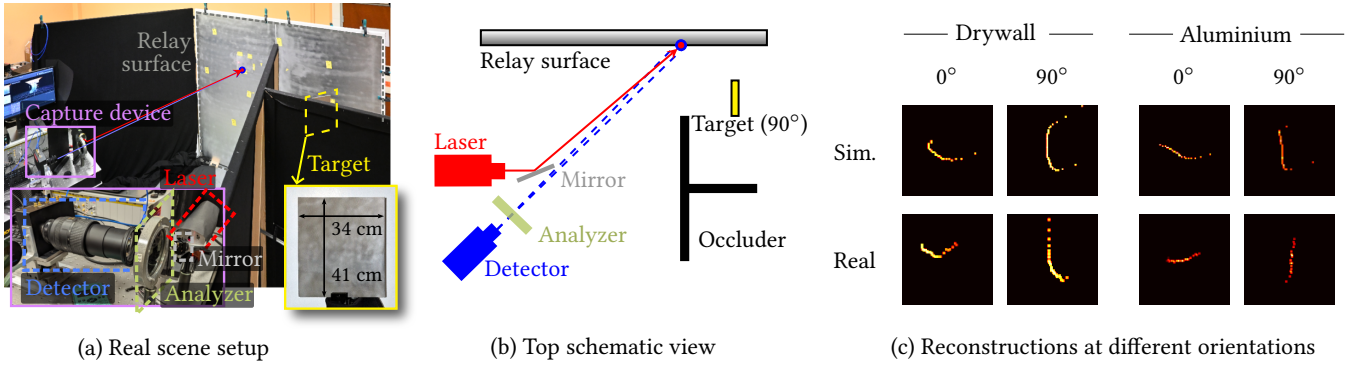


Fig. 8. (a) Our prototype NLOS setup. For our results, we capture only one point on the relay surface. (b) Top-view schematic diagram. We use aluminum for the relay surface, and tested two different materials for the target (hidden object): depolarizing drywall, and polarizing aluminum. (c) Reconstruction results (top view) for the target at  $0^\circ$  and  $90^\circ$ , the latter falling entirely in the missing cone. We compare against simulated results that closely match the actual capture conditions. Note that previous methods can not reconstruct neither at  $0^\circ$  nor  $90^\circ$ , since a single-point capture is limited to the directional ambiguities present in conventional NLOS methods (see Figure 2).

contrast, our method reconstructs such missing features in detail, even when using 16 times less scanned points.

*Additional missing cone experiments.* We next test a scene that includes the canonical, most difficult case for the missing cone problem: a plane perpendicular to the relay surface. As Figure 5 shows, as the plane’s orientation progressively places it in the missing cone, existing state-of-the-art methods fail to reconstruct it (even in a best-case, noise-free simulation setup). In contrast, our method consistently provides detailed reconstructions in all cases. Note that the recent method by Royo et al. [2023] imposes strong limitations on the hidden scenes. More specifically, it relies on auxiliary surfaces placed at particular orientations, and thus is not applicable in this scenario where no auxiliary surfaces exist.

*Analysis of glossiness.* In Figure 6 we compare our method with previous works varying the glossiness levels of both the relay surface and the target, using polarizing rough conductors with  $\alpha = 0.9$  (diffuse reflectance) and  $\alpha = 0.5$  (glossy). Our method yields consistent quality reconstructions regardless of the surface reflectance, while previous works noticeably degrade in the presence of glossy surfaces, especially the relay surface.

*Non-colliding polarization states.* Our method assumes that each time bin of the captured signal corresponds to light reflected from a single point  $x_v$  in the hidden scene. When a time bin accumulates light reflected by multiple points with similar time of flight the polarization states collide, and the recovered direction becomes a weighted sum of the directions of such points based on the reflected intensity of each point. We explore the potential of our method lifting this assumption by separating incoming light paths by their polarization state in simulation (see Supplementary for details). Decoupling incoming radiance by its polarization state allows us to distinguish points at the same distance, preventing the collision of polarization states. To illustrate the potential of this setup, we scan only *four* points  $x_l \equiv x_d$  in a  $2 \times 2$  grid on the relay surface, and exhaustively discretize the polarization dimensions into 314 angles of linear polarization  $\xi$  and 500 degrees of polarization  $\psi \in [0, 0.075]$

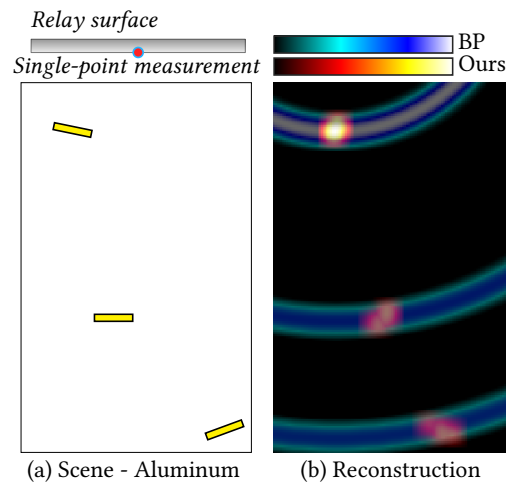


Fig. 9. Experimental capture of three planes with a single scanned point on the relay surface. (a) Top-view schematic of the experimental NLOS setup with three aluminum patches with diffuse scattering at multiple distances from the relay wall, using a single laser-SPAD measurement. (b) Superimposed reconstructions using backprojection (cool tones) and our method (warm tones). Our polarization-based method is capable of mitigating angular ambiguities that result from the lack of directionality of conventional approaches, using as few as a single captured point.

bins for each point. We evaluate the performance in the BUNNY and LUCY scenes, where some features would be invisible to previous methods, as we have seen. As shown in Figure 7, our method can reconstruct all scene features, even those in the missing cone.

## 5.2 Experimental results

Apart from the simulations, we also provide results from real captures, using our own NLOS system.

*Hardware details.* In Figure 8a we illustrate our polarization NLOS setup prototype. It uses a ps-laser source (PicoQuant, SEPIA II PDL

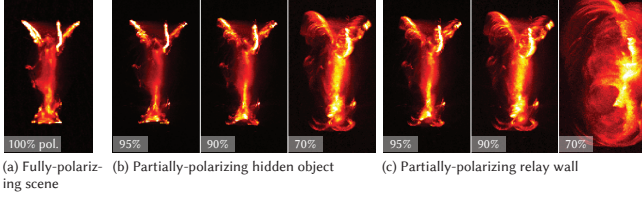


Fig. 10. (a) Our result on a fully-polarizing Lucy scene. (b, c) When the hidden scene (b) or the relay wall (c) reflect a mixture of polarized and depolarized light, the reconstruction degrades progressively as the polarizing component becomes less dominant (from 95% to 70%) due to an underestimation of the angle of incidence of light.

828-L with LDH-P-C-640B) that emits laser pulses of  $t_{p1s} = 84$  ps at a wavelength of 637 nm and a repetition rate of 10 MHz. The laser emits linearly polarized light that we can rotate using a half-wave plate. We place an analyzer between  $x_d$  and the detector to measure the four polarization angles (*Analyzer* in Figure 8a). The single photon counting detector (PhotonForce, PF32) has a focal plane array of  $32 \times 32$  SPADs which we focus into a field-of-view of about 30 milliradians on the relay surface. Each detector element can acquire information within 1024 bins at a temporal resolution of 56 ps. Thus, we can sample a transient signal of 57 ns. We average all pixels in the array to mimic a single-pixel detector. The detector is synchronized with the laser emission by a picosecond delay generator (MPD PSD-065-A-MOD). Our setup has a relatively coarse instrument response function of approximately 250 ps. We use drywall as depolarizing material (hidden object), and unpolished aluminum as polarizing material (relay surface and hidden object).

*Data acquisition.* We point the narrow detector and the laser at only one confocal scanned point. Since we rely on unpolarized light pulses but depolarizing the light emitted by the laser is impractical, we acquire two captures for each point with horizontal (Hor) and vertical (Ver) polarization instead. We capture four orientations of the analyzer ( $0^\circ$ ,  $45^\circ$ ,  $90^\circ$ , and  $135^\circ$ ) for each emitted polarization state and recover the Stokes impulse response function as:

$$H_s(x_d, t, S) = H_{\text{Hor}}(x_d, t, S) + H_{\text{Ver}}(x_d, t, S) \quad (17)$$

*Reconstruction of a plane in the missing cone.* We use our captured Stokes impulse response function to reconstruct the hidden object using our inversion method in Section 4.2. The results are shown in Figure 8c, in which we can see that the hidden plane is clearly reconstructed for both orientations ( $0^\circ$  and  $90^\circ$ ), and both polarizing and depolarizing hidden objects, despite representing challenging configurations for the missing cone problem. We remove background noise with a median filter, and high-frequency noise by subtracting a dark-count measurement followed by a Savitzky-Golay filter [1964], and compare the reconstructions of experimental data to similar simulated data.

*Reconstruction of three planes with a single captured point.* In a second scene, we validate our method with three planes placed at different depths and positions (Figure 9a). Figure 9b shows how we accurately reconstruct the position of the three planes (in warm tones) even with only a single captured point, compared with the

ambiguous results using backprojection (overlaid in cool tones), which only yields the radial distance for each plane and, thus, the resulting reconstructions are spherical manifolds of possible candidate points.

## 6 DISCUSSION AND FUTURE WORK

We have proposed a method capable of reconstructing surface features within the missing cone of NLOS imaging methods, by incorporating and leveraging polarization information. We have shown results both with polarizing depolarizing hidden objects, which illustrate the applicability of our work. While conventional methods require that the relay surface be diffuse and degrade in performance in the presence of glossy objects, we rely on a polarizing relay surface and yield consistent quality even in the presence of glossy objects. The performance of our method is affected when the hidden object or the relay wall reflect partially-polarized light. Figure 10a shows a reconstruction of Lucy with fully-polarizing hidden objects and relay wall. As we decrease the ratio of the polarization component reflected by the hidden object from 95% to 70% (Figure 10b) and increase the ratio of the depolarized component, our reconstruction result is warped and shifted laterally. A more pronounced degradation occurs when the relay wall is partially polarizing (Figure 10c). When the polarizing component becomes less dominant our method underestimates the angle of incidence of reflected light, since it depends on the degree of polarization, and, hence, the reconstruction degrades progressively.

Looking ahead, our method would be particularly well suited to be applied in NLOS systems operating at the short-wave infrared (SWIR) and near-infrared (NIR) spectral ranges [Liu et al. 2016; Oppenheim and Feiner 1995; Wang et al. 2015], since surfaces increasingly preserve polarization at such wavelengths while maintaining diffuse scattering. Given the added advantages of the SWIR and NIR spectral ranges (including eye safety), we envision future developments of SWIR and NIR laser and detector technology that will facilitate the wide adoption of polarization-based NLOS imaging.

Our technique is able to reconstruct features in the missing cone even when capturing a minimal number of points. By emitting and scanning more polarization states, combined with ellipsometry analysis-by-synthesis approaches, more accurate reconstructions could be achieved.

Last, the polarization effects of more complex real-world materials are not fully captured with single-scattering microfacet distributions. Extending our model to include more complex materials or to improve reconstructions beyond the third bounce [Royo et al. 2023; Wang et al. 2024] remains an interesting avenue of future work.

## ACKNOWLEDGMENTS

We thank the anonymous reviewers for their time and insightful comments, as well as the members of the Graphics and Imaging Lab for their help with the manuscript. Our work was funded by the European Union’s Defense Fund Program through the ENLIGHTEN project under grant agreement No. 101103242, and Oscar Pueyo-Ciudad was also partially supported by a FPU22/02432 predoctoral grant from the Ministerio de Ciencia, Innovación y Universidades.

## REFERENCES

- Byeongjoo Ahn, Akshat Dave, Ashok Veeraraghavan, Ioannis Gkioulekas, and Aswin C Sankaranarayanan. 2019. Convolutional approximations to the general non-line-of-sight imaging operator. In *Proceedings of the IEEE/CVF International Conference on Computer Vision*. IEEE, Seoul (South Korea), 7889–7899.
- Victor Arellano, Diego Gutierrez, and Adrian Jarabo. 2017. Fast back-projection for non-line of sight reconstruction. *Opt. Express* 25, 10 (2017), 11574–11583.
- Seung-Hwan Baek and Felix Heide. 2021. Polarimetric spatio-temporal light transport probing. *ACM Transactions on Graphics* 40, 6 (dec 2021), 212:1–212:18. <https://doi.org/10.1145/3478513.3480517>
- Seung-Hwan Baek and Felix Heide. 2022. All-photon Polarimetric Time-of-Flight Imaging. In *2022 IEEE/CVF Conference on Computer Vision and Pattern Recognition (CVPR)*. IEEE, New Orleans, LA, USA, 17855–17864. <https://doi.org/10.1109/CVPR52688.2022.01735>
- Petr Beckmann and André Spizzichino. 1963. The scattering of electromagnetic waves from rough surfaces. <https://api.semanticscholar.org/CorpusID:118386304>
- Martin Benning, Christoph Brune, Marinus Jan Lagerwerf, and Carola-Bibiane Schönlieb. 2015. TGV sinogram inpainting for limited angle tomography. *Proceedings of the Royal Society A* (2015).
- Katherine L. Bouman, Vickie Ye, Adam B. Yedidia, Frédo Durand, Gregory W. Wornell, Antonio Torralba, and William T. Freeman. 2017. Turning Corners into Cameras: Principles and Methods. In *2017 IEEE International Conference on Computer Vision, 2017 IEEE International Conference on Computer Vision, 2289–2297*. <https://doi.org/10.1109/iccv.2017.249>
- Mauro Buttafava, Jessica Zeman, Alberto Tosi, Kevin Eliceiri, and Andreas Velten. 2015. Non-line-of-sight imaging using a time-gated single photon avalanche diode. *Optics Express* 23, 16 (aug 2015), 20997–21011. <https://doi.org/10.1364/OE.23.020997>
- Kiseok Choi, Inchul Kim, Dongyoung Choi, Julio Marco, Diego Gutierrez, and Min H. Kim. 2023. Self-Calibrating, Fully Differentiable NLOS Inverse Rendering. In *Proceedings of ACM SIGGRAPH Asia 2023*. Association for Computing Machinery, New York, NY, USA, 11 pages.
- Alexander H Delaney and Yoram Bresler. 1998. Globally convergent edge-preserving regularized reconstruction: an application to limited-angle tomography. *IEEE Transactions on Image Processing* 7, 2 (1998), 204–221.
- Daniele Faccio, Andreas Velten, and Gordon Wetzstein. 2020. Non-line-of-sight imaging. *Nature Reviews Physics* 2, 6 (2020), 318–327. <https://doi.org/10.1038/s42254-020-0174-8> arXiv:2005.08026
- Ibón Guillén, Xiaochun Liu, Andreas Velten, Diego Gutierrez, and Adrian Jarabo. 2020. On the Effect of Reflectance on Phasor Field Non-Line-of-Sight Imaging. In *Proceedings of the IEEE International Conference on Acoustics, Speech and Signal Processing*. 9269–9273.
- Felix Heide, Matthias B Hullin, James Gregson, and Wolfgang Heidrich. 2013. Low-budget transient imaging using photonic mixer devices. *ACM Transactions on Graphics* 32, 4 (2013), 1–10.
- Felix Heide, Lei Xiao, Wolfgang Heidrich, and Matthias B. Hullin. 2014. Diffuse Mirrors: 3D Reconstruction from Diffuse Indirect Illumination Using Inexpensive Time-of-Flight Sensors. In *2014 IEEE Conference on Computer Vision and Pattern Recognition*. IEEE, Columbus, OH, USA, 3222–3229. <https://doi.org/10.1109/CVPR.2014.418>
- Julian Iseringhausen and Matthias B Hullin. 2020. Non-line-of-sight reconstruction using efficient transient rendering. *ACM Trans. Graph.* 39, 1 (2020), 1–14.
- Wenzel Jakob, Sébastien Speierer, Nicolas Russel, and Delio Vicini. 2022. DR.JIT: a just-in-time compiler for differentiable rendering. *ACM Transactions on Graphics* 41, 4 (jul 2022), 124:1–124:19. <https://doi.org/10.1145/3528223.3530099>
- Adrian Jarabo, Julio Marco, Adolfo Munoz, Raul Buisan, Wojciech Jarosz, and Diego Gutierrez. 2014. A framework for transient rendering. *ACM Transactions on Graphics* 33, 6 (2014), 1–10.
- Adrian Jarabo, Belen Masia, Julio Marco, and Diego Gutierrez. 2017. Recent advances in transient imaging: A computer graphics and vision perspective. *Visual Informatics* 1, 1 (2017), 65–79.
- Daniel S. Jeon, Andréas Meuleman, Seung-Hwan Baek, and Min H. Kim. 2023. Polarimetric iToF: Measuring High-Fidelity Depth Through Scattering Media. In *2023 IEEE/CVF Conference on Computer Vision and Pattern Recognition (CVPR)*. IEEE, Vancouver, BC, Canada, 12353–12362. <https://doi.org/10.1109/CVPR52729.2023.01189>
- Jonathan Klein, Christoph Peters, Jaime Martin, Martin Laurenzis, and Matthias B Hullin. 2016. Tracking objects outside the line of sight using 2D intensity images. *Scientific Reports* 6 (2016), 32491.
- Martin Laurenzis and Andreas Velten. 2014. Nonline-of-sight laser gated viewing of scattered photons. *Opt. Eng.* 53, 2 (2014), 023102.
- Zhengpeng Liao, Deyang Jiang, Xiaochun Liu, Andreas Velten, Yajun Ha, and Xin Lou. 2021. FPGA Accelerator for Real-Time Non-Line-of-Sight Imaging. *IEEE Transactions on Circuits and Systems I: Regular Papers* 69, 2 (2021), 721–734.
- JooWon Lim, KyeoReh Lee, Kyoung Hwan Jin, Seungwoo Shin, SeoEun Lee, YongKeun Park, and Jong Chul Ye. 2015. Comparative study of iterative reconstruction algorithms for missing cone problems in optical diffraction tomography. *Optics Express* 23, 13 (jun 2015), 16933–16948. <https://doi.org/10.1364/OE.23.016933>
- David B. Lindell, Gordon Wetzstein, and Matthew O’Toole. 2019. Wave-based non-line-of-sight imaging using fast f-k migration. *ACM Transactions on Graphics* 38, 4 (2019), 1–13.
- Fei Liu, Xiaopeng Shao, Ying Gao, Bin Xiangli, Pingli Han, and Guo Li. 2016. Polarization characteristics of objects in long-wave infrared range. *Journal of the Optical Society of America. A, Optics, image science, and vision* 33, 2 (2016), 237–43. <https://doi.org/10.1364/josaa.33.000237>
- Hao Liu, Pengfei Wang, Xin He, Mingyang Chen, Mengge Liu, Ziqin Xu, Xiaoheng Jiang, Xin Peng, and Mingliang Xu. 2023. PI-NLOS: polarized infrared non-line-of-sight imaging. *Optics Express* 31, 26 (2023), 44113–44126.
- Xiaochun Liu, Sebastian Bauer, and Andreas Velten. 2019a. Analysis of Feature Visibility in Non-Line-Of-Sight Measurements. In *2019 IEEE/CVF Conference on Computer Vision and Pattern Recognition (CVPR)*. IEEE, Long Beach, CA, USA, 10132–10140. <https://doi.org/10.1109/CVPR.2019.01038>
- Xiaochun Liu, Sebastian Bauer, and Andreas Velten. 2020. Phasor field diffraction based reconstruction for fast non-line-of-sight imaging systems. *Nature Communications* 11, 1 (2020), 1645.
- Xiaochun Liu, Ibón Guillén, Marco La Manna, Ji Hyun Nam, Syed Azer Reza, Toan Huu Le, Adrian Jarabo, Diego Gutierrez, and Andreas Velten. 2019b. Non-Line-of-sight Imaging Using Phasor-Field Virtual Wave Optics. *Nature* 572, 7771 (2019), 620–623.
- Tomohiro Maeda, Guy Satat, Tristan Swedish, Lagnojita Sinha, and Ramesh Raskar. 2019. Recent Advances in Imaging Around Corners. *arXiv preprint arXiv:1910.05613* (2019).
- Julio Marco, Adrian Jarabo, Ji Hyun Nam, Xiaochun Liu, Miguel Angel Coscolluela, Andreas Velten, and Diego Gutierrez. 2021. Virtual light transport matrices for non-line-of-sight imaging. In *2021 IEEE/CVF International Conference on Computer Vision*. 2420–2429.
- Jerome Mertz. 2019. *Introduction to Optical Microscopy* (2 ed.). Cambridge University Press.
- Fangzhou Mu, Sicheng Mo, Jiayong Peng, Xiaochun Liu, Ji Hyun Nam, Siddeshwar Raghavan, Andreas Velten, and Yin Li. 2022. Physics to the Rescue: Deep Non-line-of-sight Reconstruction for High-speed Imaging. In *IEEE Conference on Computational Photography (ICCP)*. IEEE, 1–12.
- Ji Hyun Nam, Eric Brandt, Sebastian Bauer, Xiaochun Liu, Marco Renna, Alberto Tosi, Eftychios Sifakis, and Andreas Velten. 2021. Low-latency time-of-flight non-line-of-sight imaging at 5 frames per second. *Nature Communications* 12, 1 (2021), 1–10.
- Ji Hyun Nam, Eric Brandt, Sebastian Bauer, Xiaochun Liu, Eftychios Sifakis, and Andreas Velten. 2020. Real-time Non-line-of-Sight imaging of dynamic scenes. *arXiv preprint arXiv:2010.12737* (2020).
- Uri P Oppenheim and Yoram Feiner. 1995. Polarization of the reflectivity of paints and other rough surfaces in the infrared. *Applied Optics* 34, 10 (1995), 1664. <https://doi.org/10.1364/ao.34.001664>
- Matthew O’Toole, David B. Lindell, and Gordon Wetzstein. 2018. Confocal non-line-of-sight imaging based on the light-cone transform. *Nature* 555, 7696 (2018), 338–341. <https://doi.org/10.1038/nature25489>
- Markus Plack, Clara Callenberg, Monika Schneider, and Matthias B. Hullin. 2023. Fast Differentiable Transient Rendering for Non-Line-of-Sight Reconstruction. In *2023 IEEE/CVF Winter Conference on Applications of Computer Vision (WACV)*. IEEE, Waikoloa, HI, USA, 3066–3075. <https://doi.org/10.1109/WACV56688.2023.00308>
- Joshua Rapp, Charles Saunders, Julián Tachella, John Murray-Bruce, Yoann Altmann, Jean-Yves Tourneret, Stephen McLaughlin, Robin M. A. Dawson, Franco N. C. Wong, and Vivek K. Goyal. 2020. Seeing around corners with edge-resolved transient imaging. *Nature Communications* 11, 1 (2020), 5929. <https://doi.org/10.1038/s41467-020-19727-4>
- Diego Royo, Jorge García, Adolfo Muñoz, and Adrian Jarabo. 2022. Non-line-of-sight transient rendering. *Computers & Graphics* 107 (2022), 84–92.
- Diego Royo, Talha Sultan, Adolfo Muñoz, Khadijeh Masumnia-Bisheh, Eric Brandt, Diego Gutierrez, Andreas Velten, and Julio Marco. 2023. Virtual Mirrors: Non-Line-of-Sight Imaging Beyond the Third Bounce. *ACM Transactions on Graphics (TOG)* 42, 4 (jul 2023), 140:1–140:15. <https://doi.org/10.1145/3592429>
- Charles Saunders, John Murray-Bruce, and Vivek K Goyal. 2019. Computational periscopy with an ordinary digital camera. *Nature* 565, 7740 (2019), 472–475.
- Abraham. Savitzky and M. J. E. Golay. 1964. Smoothing and Differentiation of Data by Simplified Least Squares Procedures. *Analytical Chemistry* 36, 8 (1964), 1627–1639. <https://doi.org/10.1021/ac60214a047> arXiv:https://doi.org/10.1021/ac60214a047
- Siyuan Shen, Zi Wang, Ping Liu, Zhengqing Pan, Ruiqian Li, Tian Gao, Shiyang Li, and Jingyi Yu. 2021. Non-line-of-sight imaging via neural transient fields. *IEEE Transactions on Pattern Analysis and Machine Intelligence* 43, 7 (2021), 2257–2268.
- Kenichiro Tanaka, Yasuhiro Mukaigawa, and Achuta Kadambi. 2020. Polarized Non-Line-of-Sight Imaging. In *2020 IEEE/CVF Conference on Computer Vision and Pattern Recognition (CVPR)*. IEEE, Seattle, WA, USA, 2133–2142. <https://doi.org/10.1109/CVPR42600.2020.00221>
- Antonio Torralba and William T Freeman. 2012. Accidental pinhole and pinspeck cameras: Revealing the scene outside the picture. In *2012 IEEE Conference on Computer*

- Vision and Pattern Recognition*. IEEE, Providence, RI, USA, 374–381.
- Chia-Yin Tsai, Kiriakos N Kutulakos, Srinivasa G Narasimhan, and Aswin C Sankaranarayanan. 2017. The geometry of first-returning photons for non-line-of-sight imaging. In *Proceedings of the IEEE Conference on Computer Vision and Pattern Recognition*. IEEE, Honolulu, HI, USA, 7216–7224.
- Chia-Yin Tsai, Aswin C Sankaranarayanan, and Ioannis Gkioulekas. 2019. Beyond Volumetric Albedo—A Surface Optimization Framework for Non-Line-Of-Sight Imaging. In *Proceedings of the IEEE/CVF Conference on Computer Vision and Pattern Recognition (CVPR)*. IEEE, Long Beach, CA, USA, 1545–1555.
- Andreas Velten, Thomas Willwacher, Otkrist Gupta, Ashok Veeraraghavan, Mounsi G. Bawendi, and Ramesh Raskar. 2012. Recovering three-dimensional shape around a corner using ultrafast time-of-flight imaging. *Nat. Commun.* 3, 1 (mar 2012), 745.
- Dawei Wang, Xiyang Zhi, Fanjiao Tan, Mingdong Liu, Haipeng Wang, Jinnan Gong, and Wei Zhang. 2015. Establishment and experimental verification of infrared BRDF model in rough surface. *Infrared Physics & Technology* 73 (2015), 298–303. <https://doi.org/10.1016/j.infrared.2015.10.007>
- Zewei Wang, Xiaoyin Li, Mingbo Pu, Lianwei Chen, Fei Zhang, Qi Zhang, Zhibin Zhao, Longfei Yang, Yinghui Guo, and Xiangang Luo. 2024. Vectorial-Optics-Enabled Multi-View Non-Line-Of-Sight Imaging with High Signal-To-Noise Ratio. *Laser & Photonics Reviews* (feb 2024), 2300909. <https://doi.org/10.1002/lpor.202300909> arXiv:<https://onlinelibrary.wiley.com/doi/pdf/10.1002/lpor.202300909>
- Alexander Wilkie and Andrea Weidlich. 2012. Polarised Light in Computer Graphics. In *SIGGRAPH Asia 2012 Courses* (Singapore, Singapore) (SA '12). Association for Computing Machinery, New York, NY, USA, Article 8, 87 pages. <https://doi.org/10.1145/2407783.2407791>
- Rihui Wu, Adrian Jarabo, Jinli Suo, Feng Dai, Yongdong Zhang, Qionghai Dai, and Diego Gutierrez. 2018. Adaptive polarization-difference transient imaging for depth estimation in scattering media. *Optics Letters* 43, 6 (mar 2018), 1299–1302. <https://doi.org/10.1364/OL.43.001299>
- Shumian Xin, Sotiris Nousias, Kiriakos N. Kutulakos, Aswin C. Sankaranarayanan, Srinivasa G. Narasimhan, and Ioannis Gkioulekas. 2019. A Theory of Fermat Paths for Non-Line-Of-Sight Shape Reconstruction. In *2019 IEEE/CVF Conference on Computer Vision and Pattern Recognition (CVPR)*. IEEE, Long Beach, CA, USA, 6793–6802. <https://doi.org/10.1109/CVPR.2019.00696>
- Sean I. Young, David B. Lindell, Bernd Girod, David Taubman, and Gordon Wetzstein. 2020. Non-line-of-sight Surface Reconstruction Using the Directional Light-cone Transform. In *Proc. CVPR*. IEEE, Seattle, WA, USA, 1404–1413.